Uniformity of the pseudomagnetic field in strained graphene

G. J. Verbiest, S. Brinker, and C. Stampfer

JARA-FIT and 2nd Institute of Physics, RWTH Aachen University, 52074 Aachen, Germany

We present a numerical study on the uniformity of the pseudomagnetic field in graphene as a function of the relative orientation between the graphene lattice and straining directions. We calculated the deformation of a regular micron-sized graphene hexagon by symmetrically displacing three of its edges. We found that the pseudomagnetic field is strongest if the strain is applied perpendicular to the armchair direction of graphene. For a hexagon with a side length of 1 μm, the pseudomagnetic field has a maximum of 1.2 T for an applied strain of 3.5% and it is uniform (variance <1%) within a circle with a diameter of ~520 nm. This diameter is on the order of the typical diameter of the laser spot in a state-of-the-art confocal Raman spectroscopy setup, which suggests that observing the pseudomagnetic field in measurements of shifted magnetophonon resonance is feasible.

I. INTRODUCTION

Graphene is well known for its outstanding electronic and mechanical properties as well as their remarkable coupling [1–3]. Electronically, graphene behaves as a high mobility semimetal [4], and mechanically, it is the strongest material known to mankind [5]. That graphene is a semimetal constraints the currently reachable on/off ratios for graphene transistors [6]. Therefore, much research is focused on this electromechanical coupling, as it may be utilized to tailor the electronic properties of graphene. In theory, it is even possible to get the desired electronic properties completely via so-called strain engineering [7–9]. In particular, a large mechanical deformation could induce a band gap [10–15]. However, even small deformations, or equivalently, small strain fields, already alter the electronic properties. These small deformations generate an effective potential for the charge carriers in graphene, which is similar to the vector potential of a *real* magnetic field and is therefore called the *pseudovector potential* [16–19]. In analogy to a real static magnetic field, a pseudovector potential can generate a *pseudomagnetic* field [20–22], which changes the electronic properties of graphene [23,24]. This pseudomagnetic field is always zero, unless the applied strain is *not uniform*.

A major hurdle in strain engineered graphene is the (experimental) determination of the pseudomagnetic field strength and its uniformity. Recently it was shown that the pseudomagnetic field in graphene nanobubbles can be as strong as 300 T [25], which is much stronger than one can achieve with real magnetic fields. Therefore, strained graphene offers the unique opportunity to study the electronic properties of graphene at extreme (pseudo)magnetic field strengths. Alternatively, such systems could allow studies to the magnetophonon resonance in Raman spectroscopy [26] or enable so-called valleytronics [27–30], or enable strain tunable pseudomagnetic quantum dots [31,32]. Numerical work of strain fields in graphene is therefore of additional value, as it not only estimates the strength of the pseudomagnetic field, but also shows the uniformity of the generated pseudomagnetic field and its dependence on the lattice orientation with respect to the strain direction.

Very recently, microelectromechanical systems (MEMS) have been introduced, which could allow for triaxial in-plane strain fields in suspended graphene [33–35]. This makes it possible to study the effect of strain on graphene experimentally, without having to deal with the effects of a substrate. Substrates are known to introduce both out-of-plane, e.g., ripples and small bumps, as well as in-plane strain variations and thereby induce a pseudomagnetic field. It has been shown that these type of out-of-plane and in-plane distortions are of extreme importance for the transport properties of high-quality graphene [36–38]. As these MEMS devices strain suspended graphene flakes in-plane, we do not consider the complex interplay between in-plane and out-of-plane strain.

In this paper we show calculations of the pseudomagnetic field in a regular hexagon of graphene that is strained simultaneously in three different in-plane directions. As the uniformity of the pseudomagnetic field determines whether it is detectable with a local probe, e.g., a scanning tunneling microscope cantilever [39] or a laser probe, we specifically study this as a function of the lattice orientation. For this we consider two hexagonal geometries with side length L of 100 nm and 1 μm, respectively. We show that the pseudomagnetic field is constant within a circle of diameter d that strongly depends on the relative orientation between the graphene lattice and the strain direction. For the hexagonal geometry with $L = 1$ μm, we find a diameter d of around 520 nm. In addition, we show that a special geometry, which was believed to generate a uniform pseudomagnetic field for a specific strain field [40], actually does not do so. Finally, we show that an uniform pseudomagnetic field can indeed be generated by applying a linearly varying force on two opposing edges of a rectangle [41].

This paper is organized as follows. First, we describe the theoretical origin of the pseudomagnetic field. Second, we discuss the methods that we used to calculate the pseudomagnetic field. Then we show our results before finishing with the experimental implications and the conclusion.

II. THE PSEUDOMAGNETIC FIELD

The electronic structure of graphene is described by a tight-binding Hamiltonian which only takes the interaction of the π states into account [4]:

$$H = -\sum_{n=1}^{3} t_n \begin{pmatrix} 0 & e^{-i\mathbf{k}\cdot\mathbf{d_n}} \\ e^{i\mathbf{k}\cdot\mathbf{d_n}} & 0 \end{pmatrix}, \quad (1)$$
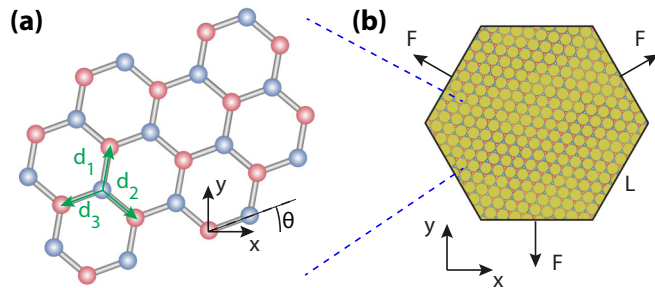
FIG. 1. (Color online) (a) The lattice structure of graphene, in which θ indicates the rotation angle between the armchair direction and the x axis. The red and blue atoms indicate the two different sublattices, and the $\mathbf{d_n}$ indicates the nearest neighbor vectors. (b) The geometry used in our calculations is a regular hexagon with side length L. The force F is applied to the indicated edges.

in which $\mathbf{k}$ is the momentum of the electron, $\{\mathbf{d_n}\}$ are the three nearest neighbor vectors [see Fig. 1(a)], and $\{t_n\}$ are the corresponding nearest neighbor hopping parameters. This Hamiltonian is a 2×2 matrix, as each unit cell of graphene contains two carbon atoms. As Fig. 1(a) shows, each of these atoms forms a sublattice. The energy spectrum corresponding to Eq. (1) contains six specific electron momenta $\mathbf{k}$, for which the energy is zero. These six points are characterized by only two momenta: $\mathbf{K}$ and $\mathbf{K'}$, which is a consequence of the underlying sublattice symmetry.

The nearest neighbor hopping parameters $\{t_n\}$ change under a deformation of the graphene lattice, as such a deformation changes the nearest neighbor distance. The change in hopping parameters is described by

$$t_n = t_0 e^{-\beta(|\mathbf{d_n}|/a-1)}, \quad (2)$$

in which a is the nearest neighbor distance without any deformation, $t_0 \approx 2.8$ eV is the hopping parameter without any deformation, and $\beta \approx 2$–3.37 is the Grüneisen parameter [11,42–44]. The parametrization of the hopping parameter t_n in Eq. (2) is in agreement with full DFT calculations up to strain values of at least 10% [45]. As a consequence, this also holds for the tight-binding approximation which we employ. For the calculations below, we follow [11,44] and use a Grüneisen parameter of $\beta = 3.37$.

In case of zero strain ($|\mathbf{d_n}| = a \, \forall n$), one can make the usual expansion around the $\mathbf{K}$ point for low energy electrons ($\mathbf{k} = \mathbf{K} + \boldsymbol{\kappa}$), to find a Hamiltonian that is linear in $\boldsymbol{\kappa}$,

$$H = \hbar v_{\mathrm{F}} \boldsymbol{\sigma} \cdot \boldsymbol{\kappa}, \quad (3)$$

where $v_{\mathrm{F}} = 3at_0/2\hbar$ is the Fermi velocity, and $\boldsymbol{\sigma} = (\sigma_x, \sigma_y)$ are the Pauli matrices.

In the case of nonzero strain, one finds a similar expression for the Hamiltonian by using $\delta t_n = t_n - t_0$. In fact, one finds the same Hamiltonian as in Eq. (3), but with an additional term that is independent of the momentum $\boldsymbol{\kappa}$:

$$H = \hbar v_{\mathrm{F}} \sigma \cdot (\boldsymbol{\kappa} - e\mathbf{A}), \quad (4)$$

in which e is the electron charge, and $\mathbf{A} = (A_x, A_y)$ is the so-called pseudovector potential,

$$A_x + i A_y = -\frac{1}{ev_{\mathrm{F}}} \sum_{n=1}^{3} \delta t_n e^{-i\mathbf{K} \cdot \mathbf{d_n}}. \quad (5)$$

Equation (4) immediately explains why $\mathbf{A}$ is called a pseudovector potential, as the additional term in H mimics the vector potential of a real magnetic field. Therefore, we define, in analogy to a real magnetic field, a pseudomagnetic field:

$$B = \frac{\partial A_y}{\partial x} - \frac{\partial A_x}{\partial y}. \quad (6)$$

However, there is one remarkable difference: B changes sign, if one expands the Hamiltonian around the $\mathbf{K'}$ point instead of the $\mathbf{K}$ point. Consequently, the electrons in the two valleys feel an opposite magnetic field [22]. This property is important for valleytronics since it may allow us to make valley filters [27–30].

III. ROTATION OF THE LATTICE RELATIVE TO THE STRAIN DIRECTION

It is a convention to define an angle θ as the angle between the x axis and the so-called armchair direction of graphene [see Fig. 1(a)]. If $\theta = 0$ and the displacements $|\mathbf{u}|$ are much smaller than a, it is well known that the pseudovector potential can be written in terms of the deformation tensor u_{ij} [$i, j = (x, y)$] [16,46],

$$A_x = \frac{\hbar\beta}{2ae}(u_{xx} - u_{yy}), \quad (7)$$

$$A_y = \frac{\hbar\beta}{2ae}(-2u_{xy}), \quad (8)$$

in which $u_{ij} = \frac{1}{2}(\frac{\partial u_i}{\partial j} + \frac{\partial u_j}{\partial i})$.

We now rotate the lattice with respect to the x axis by an angle θ [see Fig. 1(a)] using the standard rotation matrix R in two dimensions:

$$R = \begin{pmatrix} \cos\theta & -\sin\theta \\ \sin\theta & \cos\theta \end{pmatrix}. \quad (9)$$

We note that $\mathbf{K} \cdot \mathbf{d_n}$ is constant under lattice rotations, which implies that the usual derivation of Eqs. (7) and (8) still holds. Therefore, we only need to find the deformation tensor for the rotated lattice [40], before we rotate the pseudovector potential $\mathbf{A}$:

$$\begin{pmatrix} u_{x'x'} & u_{x'y'} \\ u_{x'y'} & u_{y'y'} \end{pmatrix} = \mathcal{R} \begin{pmatrix} u_{xx} & u_{xy} \\ u_{xy} & u_{yy} \end{pmatrix} \mathcal{R}^T \quad (10)$$

and

$$\begin{pmatrix} A_x \\ A_y \end{pmatrix} = \begin{pmatrix} \cos\theta & \sin\theta \\ -\sin\theta & \cos\theta \end{pmatrix} \begin{pmatrix} A_{x'} \\ A_{y'} \end{pmatrix}. \quad (11)$$

Substituting Eqs. (10) and (11) into Eqs. (7) and (8), we find an expression for the pseudovector potential for arbitrary lattice rotations [40]:

$$A_x = \frac{\hbar\beta}{2ae}[(u_{xx} - u_{yy})\cos(3\theta) - 2u_{xy}\sin(3\theta)], \quad (12)$$

$$A_y = -\frac{\hbar\beta}{2ae}[(u_{xx} - u_{yy})\sin(3\theta) + 2u_{xy}\cos(3\theta)]. \quad (13)$$

Considering the pseudomagnetic field, one sees that it has a rotational symmetry of 120°. A rotation of the graphene lattice by an angle of 120° gives the same pseudomagnetic field and a

rotation of 60° effectively changes the sign. This implies that the pseudomagnetic field is zero for an angle of 30°.

IV. METHODS

We define a hexagonal geometry with side length L, as shown in Fig. 1(b), of which the orientation is always kept constant. It is only the lattice orientation of the graphene that is rotated with respect to the x axis. In order to calculate the pseudomagnetic field we make use of a two-step approach.

In the first step we calculate the deformation of the geometry in COMSOL [47] using a triangular mesh, for which we consider only in-plane strain as well as only the *linear* contributions to elasticity theory. For this calculation we assumed that graphene has a thickness of 3.35 Å, a Young's modulus of 1.02 TPa, and a Poisson's ration of 0.165 [5,48]. The strain is applied via a fixed displacement of 10 nm of the three edges that are indicated with arrows in Fig. 1(b) in all calculations. As a consequence, these three edges or boundaries have a fixed displacement during the entire calculation. In contrast, the other three edges are free. This type of boundary condition is known to break the sublattice symmetry and thus opens a band gap [49]. From the calculated deformation field, we export the displacement vectors at the position of the atoms for the second step, in which we calculate both the pseudovector potential and the pseudomagnetic field. Alternatively, one can directly export the deformation matrix and use Eqs. (12) and (13). We used this to crosscheck our results obtained via the displacement vectors and we found that the method using the deformation matrix overestimates the strength of the pseudomagnetic field. This overestimation arises from the fact that Eqs. (12) and (13) are obtained by assuming a linear change in hopping parameters t_n with strain. For the structure discussed in Fig. 2 and a strain of 10%, this overestimation is even almost 30% and is in agreement with previously reported work [20].

V. RESULTS

Let us start with a hexagonal geometry of $L = 100$ nm. Figure 2(a) shows the strain obtained by applying a fixed displacement of 10 nm to the three edges for zero rotation angle ($\theta = 0$). As three sides have a fixed displacement, the side length L of those particular sides is fixed to that of the undeformed geometry. In contrast, the side lengths of the other sides *are* allowed to change. This exactly leads to the strain pattern that we observe: zero strain along three edges at which we apply the fixed displacement and a finite strain (15%) along the other three edges. For the same reason, the strain is highest at the six corners of the geometry (up to 50%). Note that this 50% of strain will not be reached in an experimental situation, as the corners will not be so sharp and the boundary condition will not be so rigid. In the center of the geometry, the strain reduces to 0%. This is due to the symmetry of the applied fixed displacements, as the (vector) sum of them is zero.

The panels in Fig. 2(b) show the pseudomagnetic field for rotation angles θ varying from 0 to 30 deg. A positive (negative) pseudomagnetic field is indicated in red (blue). We
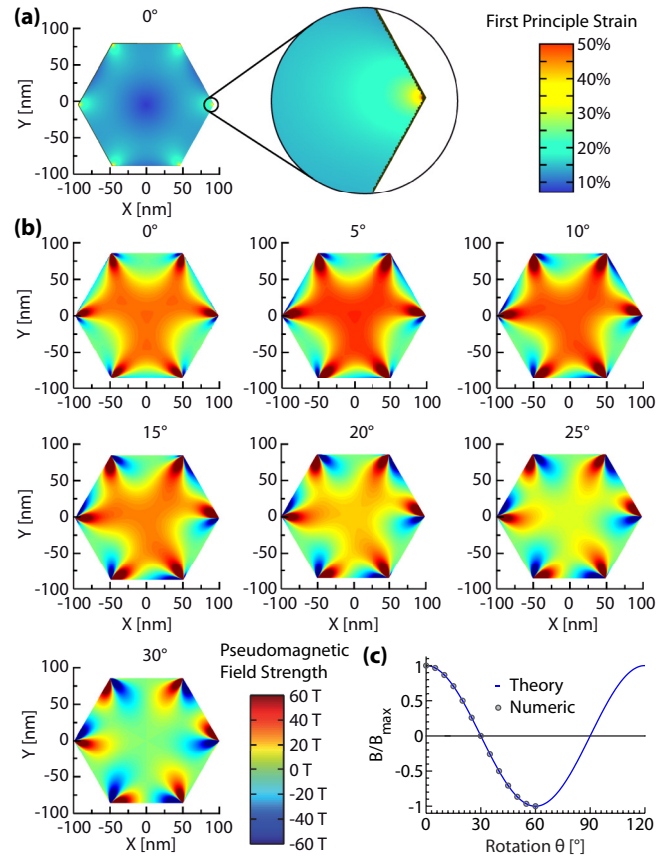

FIG. 2. (Color online) (a) The strain in the geometry for zero rotation angle θ. There are three edges with zero strain and three with 15% of strain. The corners of the geometry exhibit the largest amount of strain (up to 50%), whereas the strain reduces to 0% in the center. (b) The pseudomagnetic field as a function of the rotation angle θ. At $\theta = 30°$ the pseudomagnetic field disappears in the center of the geometry, as the atomic displacement is parallel to the nearest neighbor vectors. (c) The pseudomagnetic field in the center of the geometry is in excellent agreement with that from Eqs. (12) and (13). The pseudomagnetic field is normalized with respect to the field at $\theta = 0°$.

observe two contributions to the total pseudomagnetic field: the one at the six corners of the hexagon and the one from the center of the geometry. The pseudomagnetic field at the corners does not change when rotating the graphene lattice. It remains constant with values around $+60$ and -60 T. The origin of this pseudomagnetic field is our boundary condition (see above). As a consequence, we get a large relative displacement at the six corners of the geometry, which results in the observed pseudomagnetic field.

In contrast, the pseudomagnetic field in the center of the geometry does depend on the rotation angle θ. The maximum pseudomagnetic field B_{max} in the center of the geometry is around 40 T for $\theta = 0°$ and decreases rapidly when increasing the rotation angle θ. At a rotation angle of $\theta = 30°$, the pseudomagnetic field in the center of the geometry is even *zero*, as the atomic displacement is parallel to the nearest neighbor vectors. Figure 2(c) shows the pseudomagnetic field in the center of the geometry normalized by B_{max} as a function of
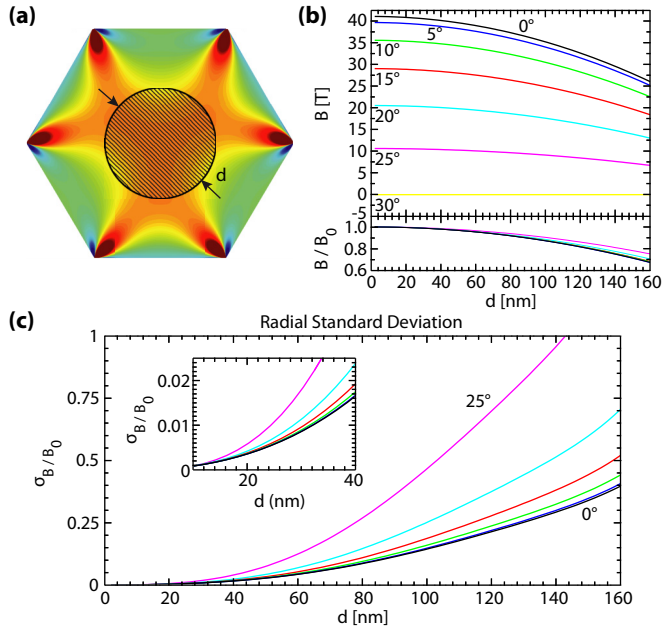
FIG. 3. (Color online) (a) The average pseudomagnetic field and its corresponding normalized standard deviation are calculated within a circle of diameter d that is centered in the geometry. (b) The upper panel shows the pseudomagnetic field as a function of the diameter d for different rotation angles. The bottom panel shows that all these curves fall almost on top of each other if one normalizes each curve with respect to the value of the pseudomagnetic field in the center. (c) The standard deviation of the pseudomagnetic field as a function of the diameter d for the rotation angles shown in (b). The generated pseudomagnetic field is uniform within $d = 34$ nm for $\theta = 0°$. The inset shows a zoom for small d.

the rotation angle θ as well as the normalized pseudomagnetic field that one obtains from Eqs. (12) and (13). As Fig. 2(c) shows, our numerical calculation is in perfect agreement with the theoretical prediction.

The uniformity of the pseudomagnetic field is of crucial importance for the possible utilization of it in experiments and devices. To quantify the uniformity of the pseudomagnetic field B, we calculate the average value of B in a circle of diameter d that is centered in the geometry [see Fig. 3(a)]. The result is shown in the upper panel of Fig. 3(b) for various rotation angles θ. In order to compare the uniformity of the pseudomagnetic field at different rotation angles θ, we normalize each curve with respect to the pseudomagnetic field B_0 at $d = 2$ nm [see the lower panel of Fig. 3(b)]. It should be noted that the curves for different θ are very similar and only deviate for large d. Finally, Fig. 3(c) shows the standard deviation of the normalized pseudomagnetic field σ_{B/B_0} as a function of d. To characterize the homogeneous area of the pseudomagnetic field one has to set an upper limit on the standard deviation. We choose a standard deviation smaller than 1% of the maximum pseudomagnetic field in the center. By using this definition, we obtain a diameter of uniformity of around 34 nm for $\theta = 0$.

Figure 4(a) shows an overview of a feasible MEMS actuator that allows us to experimentally strain grapheme sheets. The arms of the MEMS actuator are placed under an angle
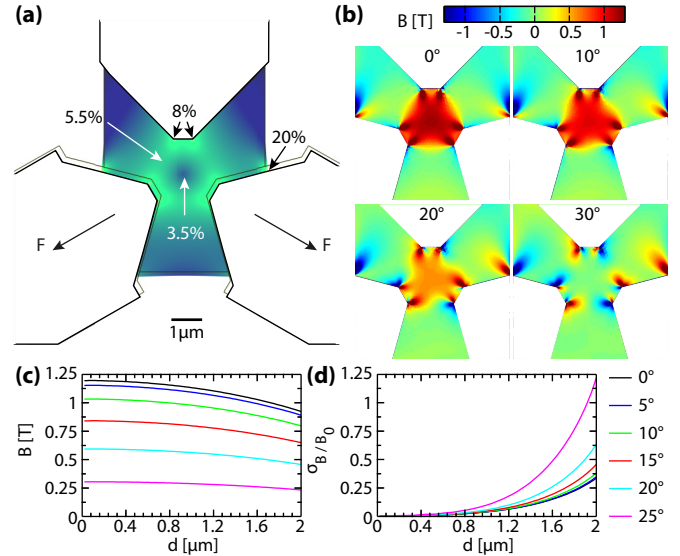

FIG. 4. (Color online) (a) The computed strain field in a graphene sheet that can be reached with a state-of-the-art MEMS device shows values (∼20%) close to the maximum strain that graphene can withstand. The force F is applied to the indicated edges. (b) The corresponding pseudomagnetic field for various rotation angles θ. (c) The pseudomagnetic field as a function of d and (d) the corresponding standard deviation. In this case, the pseudomagnetic field is uniform within $d = 520$ nm.

of 120 deg and are connected with a rectangular sheet of graphene, which has a width of 5 μm and a length of 7 μm. This configuration generates a force field which has the same threefold symmetry as for the hexagonal structure above [see Fig. 1(c)]. However, the effective side length is now ∼1 μm. The strain in the graphene sheet resulting from the same fixed displacement as before is shown in Fig. 4(a). Although the strain in the center region of the geometry is on average 3.5%, the maximum strain value is 8% on the corners of the hexagon and 5.5% on the sides. The maximum strain in the entire geometry occurs at the positions where the graphene/MEMS device boundary has a corner. At these locations, the strain is even around 20%, which is the amount of strain at which the graphene sheet is supposed to start to rupture [5,50]. Nevertheless, it is expected that such high strain values will not be reached in an experiment.

The pseudomagnetic field for different rotation angles of the lattice with respect to the strain directions is calculated and depicted in Fig. 4(b). The pseudomagnetic field has the same characteristics as the pseudomagnetic field of the strained hexagon in Fig. 2. The strength of the pseudomagnetic field is highest in each corner of the hexagon and the field in the center is strongest for $\theta = 0$. Figure 4(c) shows the strength of the pseudomagnetic field as a function of the diameter d of a circle that is placed identically to that in Fig. 3(a). For $\theta = 0$ the pseudomagnetic field is approximately 1.2 T in the center. If we compare this with the maximum pseudomagnetic field in the hexagon with side length $L = 100$ nm, we see that it is approximately 30 times weaker. This is due to the following two effects. First, by increasing the side length L by a factor of 10, the gradient in the pseudovector potentials is 10 times

smaller, which results in a 10 times smaller pseudomagnetic field. Second, the applied strain is now approximately ∼3.5%, which is approximately 3 times smaller than the 10% that we had before. Combining both explains the ∼30 times weaker pseudomagnetic field.

If we now consider the uniformity of the pseudomagnetic field in such MEMS devices, as shown in Fig. 4(d), we obtain a diameter of uniformity of around 520 nm for $\theta = 0°$. If we would choose a standard deviation smaller than 5% of the maximum pseudomagnetic field in the center of the geometry, the diameter of uniformity increases to ∼1100 nm for $\theta = 0°$. As both values are comparable to the typical laser spot size in state-of-the-art confocal Raman spectroscopy experiments, it may be possible to quantify the pseudomagnetic field strength in an experiment as it induces a shift in the MPR [51]. In addition, it may be possible to measure the strength of the pseudomagnetic field via its effect on the quantum Hall plateaus [52].

Apart from the experimentally accessible geometries that we discussed so far, certain geometries with corresponding force fields have been suggested that should give rise to a completely uniform pseudomagnetic field. In particular, Guinea *et al.* [40] give two of such (analytic) geometries with corresponding force fields. Using our approach, we confirmed the uniform pseudomagnetic field in the circular disk for the displacement field given in Ref. [40]. Let us next focus on the second geometry given in Ref. [40]. This geometry should give an uniform pseudomagnetic field when only perpendicular forces are applied to its boundary. The analytic expression for this geometry in polar coordinates is derived under the assumption of pure shear stresses (see the Supplementary Information of [40]):

$$r(\phi) = \frac{c}{[(\cos\phi/2 \mp \sin\phi/2)(\pm 1 + 2\sin\phi)]^{2/3}}. \quad (14)$$

In this equation, r is the radius, ϕ is the polar angle, and c is a constant. The $\pm$ sign indicates two equivalent geometries that are rotated by 60 deg with respect to each other. It does not matter which sign we take, the radius always becomes imaginary for specific angles. For simplicity we choose the $+$ sign for our geometry. Figure 5(a) shows both the real part (black) and imaginary part (red) of the radius r as a function of the angle ϕ for $c = 1 \, \mu m$. Please realize that $r(\phi)$ is imaginary and, therefore, physically *not* allowed. We can obtain the geometry shown in [40] by taking the absolute value of $r(\phi)$ [see Fig. 5(b)]. However, if we calculate the pseudomagnetic field for this given geometry and force field using our numerical approach, we observe that it is not uniform [see Fig. 5(c)]. However, in the arms of this geometry, the pseudomagnetic field looks almost uniform. Based on this, it can be shown that a rectangle with linearly varying forces perpendicular to two opposing boundaries [see left panel in Fig. 5(d)] does give rise to an uniform pseudomagnetic field [41]. The corresponding strain and deformation of a geometry with a side length of 200 nm is shown in the right panel of Fig. 5(d). The maximum force per unit length used in this calculation was 60 N/m, which resulted in an uniform pseudomagnetic field of 8 T.
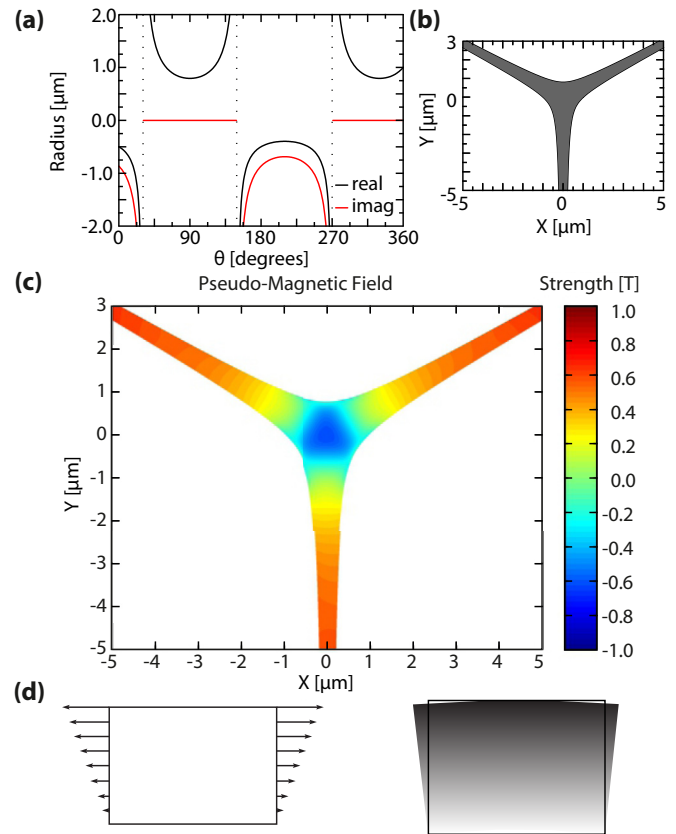

FIG. 5. (Color online) The solution for the radius r for $c = 1 \, \mu m$ as a function of the angle θ (a) and its corresponding geometry for $|r|$ (b). In contrast to what was thought, the resulting pseudomagnetic field is not uniform (c). (d) The linearly varying forces (left panel) on two opposing boundaries of a rectangle that generate a uniform pseudomagnetic field. The right panel shows the strain in a grayscale as well as the resulting shape of the geometry.

VI. EXPERIMENTAL IMPLICATIONS

A particular experiment, in which the strength of a tunable pseudomagnetic field may be directly probed, is the shift of the magnetophonon resonance (MPR) in Raman spectroscopy [51,53–56]. In order to exclude other effects, the pseudomagnetic field must be uniform within the laser spot size in the confocal Raman spectroscopy experiment, which is exactly what we showed and discussed in this paper. By following the recent experiment of Neumann *et al.* [26], where MPRs at low magnetic fields have been observed, we can estimate the experimental requirements for observing MPR shifts thanks to a tunable pseudomagnetic field. The most prominent MPR below 20 T is the so-called T_1 transition at around 3.7 T, which results in a well resolved peak of the Raman G linewidth as a function of magnetic field. This resonance peak has an experimentally observed peak linewidth (FWHM) of around 700 mT. We assume that at least a peak shift of half the linewidth of this magnetophonon resonance is needed for unambiguously proving the presence of a pseudomagnetic field. In addition, we have to take into account the effect of strain on the Raman G line itself. It is known that the Raman G line shifts with increasing strain and, for moderate uniaxial strain, even splits into a so-called

G^+ and G^- line [57–59]. The G^+ line corresponds to a phonon parallel to the direction of strain and the G^- line to one perpendicular. Therefore, there is no Raman G-line splitting for pure biaxial strain [60–63]. In our case, the strain profile shown in Fig. 4 has approximately radial symmetry. Therefore, the G^- line does not shift and the G^+ line shifts with -10.8 cm^{-1}/%. The average strain in the circular region seen by the Raman laser is 2/3 of the maximum strain ϵ_{max}. As a result, the frequency difference between the G^- line and the G^+ line is around $7.2\epsilon_{max}$. This means that the Raman G line is expected to broaden by $3.6\epsilon_{max}$, which corresponds to a broadening of 40% per percent strain. Assuming that the MPR broadens by the same amount, we need a strain of 1.67% to see a splitting of the MPR due to the pseudomagnetic field. Note that for this strain value, the G^+ line and G^- line still appear as a single peak. These values are by a factor 2 below the values discussed above [see Fig. 4(a)] allowing for a nonperfect lattice alignment and making this approach promising for investigating tunable pseudomagnetic fields.

VII. CONCLUSION

We studied the strength and uniformity of the pseudomagnetic field in a hexagonal sheet of graphene as a function of the rotation angle θ between the armchair direction of

graphene and the strain direction. We showed that the relative orientation of the graphene lattice with respect to the strain direction is extremely important, as the pseudomagnetic field even disappears for specific angles. The pseudomagnetic field is strongest when the strain is parallel to the armchair direction in the graphene. To characterize the homogeneous area of the pseudomagnetic field, we set an upper limit on the standard deviation in the pseudomagnetic field of 1%. Using this definition, the pseudomagnetic field is constant within a diameter of ∼520 nm for a hexagonal graphene sheet with a side length of 1 μm. Our results show that the pseudomagnetic field is detectable with a local probe such as a scanning tunneling microscope cantilever but even also with a typical confocal laser probe. One may even think of observing a shift in the magnetophonon resonance due to the strain-induced pseudomagnetic field. In addition, tunable pseudomagnetic fields are important for valleytronics since they may allow us to make valley filters.

ACKNOWLEDGMENTS

[1] M. Huang, T. A. Pascal, H. Kim, W. A. Goddard, and J. R. Greer, Nano Lett. **11**, 1241 (2011).

[2] M. Trif, P. Upadhyaya, and Y. Tserkovnyak, Phys. Rev. B **88**, 245423 (2013).

[3] T. Mashoff, M. Pratzer, V. Geringer, T. J. Echtermeyer, M. C. Lemme, M. Liebmann, and M. Morgenstern, Nano Lett. **10**, 461 (2010).

[4] M. I. Katsnelson, *Graphene: Carbon in Two Dimensions* (Cambridge University Press, New York, 2012).

[5] C. Lee, X. Wei, J. W. Kysar, and J. Hone, Science **321**, 385 (2008).

[6] F. Xia, D. B. Farmer, Y-M. Lin, and P. Avouris, Nano Lett. **10**, 715 (2010).

[7] V. M. Pereira and A. H. Castro Neto, Phys. Rev. Lett. **103**, 046801 (2009).

[8] T. Low and F. Guinea, Nano Lett. **10**, 3551 (2010).

[9] B. Amorim, A. Cortijo, F. de Juan, A. G. Grushin, F. Guinea, A. Gutirrez-Rubio, H. Ochoa, V. Parente, R. Roldn, P. San-Jos, J. Schiefele, M. Sturla, and M. A. H. Vozmediano, arXiv:1503.00747.

[10] Y. Hasegawa, R. Konno, H. Nakano, and M. Kohmoto, Phys. Rev. B **74**, 033413 (2006).

[11] V. M. Pereira, A. H. Castro Neto, and N. M. R. Peres, Phys. Rev. B **80**, 045401 (2009).

[12] F. M. D. Pellegrino, G. G. N. Angilella, and R. Pucci, Phys. Rev. B **81**, 035411 (2010).

[13] G. Cocco, E. Cadelano, and L. Colombo, Phys. Rev. B **81**, 241412(R) (2010).

[14] S.-M. Choi, S.-H. Jhi, and Y.-W. Son, Phys. Rev. B **81**, 081407(R) (2010).

[15] S.-S. Choi, S.-H. Jhi, and Y.-W. Son, Nano Lett. **10**, 3486 (2010).

[16] H. Suzuura and T. Ando, Phys. Rev. B **65**, 235412 (2002).

[17] K-I. Sasaki, Y. Kawazoe, and R. Saito, Prog. Theor. Phys. **113**, 463 (2005).

[18] M. I. Katsnelson and K. S. Novoselov, Solid State Commun. **143**, 3 (2007).

[19] F. de Juan, J. L. Mañes, and María A. H. Vozmediano, Phys. Rev. B **87**, 165131 (2013).

[20] M. R. Masir, D. Moldovan, and F. M. Peeters, Solid State Commun. **175-176**, 76 (2013).

[21] N. Abedpour, R. Asgari, and F. Guinea, Phys. Rev. B **84**, 115437 (2011).

[22] K.-J. Kim, Ya. M. Blanter, and K.-H. Ahn, Phys. Rev. B **84**, 081401(R) (2011).

[23] L. G. da Silva Leite, C. Filgueiras, D. Cogollo, and E. O. Silva, Phys. Lett. A **379**, 907 (2015).

[24] M. Schneider, D. Faria, S. V. Kusminskiy, and N. Sandler, Phys. Rev. B **91**, 161407(R) (2015).

[25] N. Levy, S. A. Burke, K. L. Meaker, M. Panlasigui, A. Zettl, F. Guinea, A. H. Castro Neto, and M. F. Crommie, Science **329**, 544 (2010).

[26] C. Neumann, S. Reichardt, M. Drögeler, K. Watanabe, T. Taniguchi, B. Beschoten, S. V. Rotkin, and C. Stampfer, Nano Lett. **15**, 1547 (2015).

[27] A. Rycerz, J. Tworzydlo, and C. W. J. Beenakker, Nat. Phys. **3**, 172 (2007).

[28] M. H. D. Guimaraes, A. Veligura, P. J. Zomer, T. Maassen, I. J. Vera-Marun, N. Tombros, and B. J. van Wees, Nano Lett. **2012**, 3512 (2012).

[29] Y. Jiang, T. Low, K. Chang, M. I. Katsnelson, and F. Guinea, Phys. Rev. Lett. **110**, 046601 (2013).

[30] M. M. Grujic, M. Z. Tadic, and F. M. Peeters, Phys. Rev. Lett. **113**, 046601 (2014).

[31] Z. Qi, D. A. Bahamon, V. M. Pereira, H. S. Park, D. K. Campbell, and A. H. Castro Neto, Nano Lett. **13**, 2692 (2013).

[32] D. A. Bahamon, Z. Qi, H. S. Park, V. M. Pereira, and D. K. Campbell, arXiv:1503.08488.

[33] H. H. P. Garza, E. W. Kievit, G. F. Schneider, and U. Staufer, Nano Lett. **14**, 4107 (2014).

[34] H. H. P. Garza, E. W. Kievit, G. F. Schneider, and U. Staufer, Nanotechnology **25**, 465708 (2014).

[35] H. Zhang, J.-W. Huang, J. Velasco, Jr., K. Myhro, M. Maldonado, D. D. Tran, Z. Zhao, F. Wang, Y. Lee, G. Liu, W. Bao, and C. N. Lau, Carbon **69**, 336 (2014).

[36] R. Carrillo-Bastos, D. Faria, A. Latge, F. Mireles, and N. Sandler, Phys. Rev. B **90**, 041411(R) (2014).

[37] D. Moldovan, M. R. Masir, and F. M. Peeters, Phys. Rev. B **88**, 035446 (2013).

[38] J. V. Sloan, A. A. P. Sanjuan, Z. Wang, C. Horvath, and S. Barraza-Lopez, Phys. Rev. B **87**, 155436 (2013).

[39] J.-F. Liu, K.-K. Bai, J.-B. Qiao, Y. Zhou, J.-C. Nie, H. Peng, Z. Liu, and L. He, arXiv:1503.08392.

[40] F. Guinea, M. I. Katsnelson, and A. K. Geim, Nat. Phys. **6**, 30 (2010).

[41] F. Guinea, A. K. Geim, M. I. Katsnelson, and K. S. Novoselov, Phys. Rev. B **81**, 035408 (2010).

[42] A. J. Heeger, S. Kivelson, J. R. Schrieffer, and W-P. Su, Rev. Mod. Phys. **60**, 781 (1988).

[43] M. A. H. Vozmediano, M. I. Katsnelson, and F. Guinea, Phys. Rep. **496**, 109 (2010).

[44] A. H. Castro Neto and F. Guinea, Phys. Rev. B **75**, 045404 (2007).

[45] R. M. Ribeiro, V. M. Pereira, N. M. R. Peres, P. R. Briddon, and A. H. Castro Neto, New J. Phys. **11**, 115002 (2009).

[46] J. L. Mañes, Phys. Rev. B **76**, 045430 (2007).

[47] http://www.comsol.com.

[48] O. L. Blakslee, D. G. Proctor, E. J. Seldin, G. B. Spence, and T. Weng, J. Appl. Phys. **41**, 3373 (1970).

[49] M. Neek-Amal, L. Covaci, Kh. Shakouri, and F. M. Peeters, Phys. Rev. B **88**, 115428 (2013).

[50] K. S. Kim, Y. Zhao, H. Jang, S. Y. Lee, J. M. Kim, K. S. Kim, J.-H. Ahn, P. Kim, J.-Y. Choi, and B. H. Hong, Nature (London) **457**, 706 (2009).

[51] M. Assili, S. Haddad, and W. Kang, Phys. Rev. B **91**, 115422 (2015).

[52] B. Roy, Z.-X. Hu, and K. Yang, Phys. Rev. B **87**, 121408(R) (2013).

[53] M. O. Goerbig, J.-N. Fuchs, K. Kechedzhi, and V. I. Fal'ko, Phys. Rev. Lett. **99**, 087402 (2007).

[54] C. Faugeras, M. Amado, P. Kossacki, M. Orlita, M. Kuhne, A. A. L. Nicolet, Yu. I. Latyshev, and M. Potemski, Phys. Rev. Lett. **107**, 036807 (2011).

[55] S. Goler, J. Yan, V. Pellegrini, and A. Pinczuk, Solid State Commun. **152**, 1289 (2012).

[56] C. Faugeras, P. Kossacki, A. A. L. Nicolet, M. Orlita, M. Potemski, A. Mahmood, and D. M. Basko, New J. Phys. **14**, 095007 (2012).

[57] T. M. G. Mohiuddin, A. Lombardo, R. R. Nair, A. Bonetti, G. Savini, R. Jalil, N. Bonini, D. M. Basko, C. Galiotis, N. Marzari, K. S. Novoselov, A. K. Geim, and A. C. Ferrari, Phys. Rev. B **79**, 205433 (2009).

[58] Z. H. Ni, T. Yu, Y. H. Lu, Y. Y. Wang, Y. P. Feng, and Z. X. Shen, ACS Nano **2**, 2301 (2008).

[59] M. Huang, H. Yan, C. Chen, D. Song, T. F. Heinz, and J. Hone, Proc. Natl. Acad. Sci. USA **106**, 7304 (2009).

[60] F. Ding, H. Ji, Y. Chen, A. Herklotz, K. Dorr, Y. Mei, A. Rastelli, and O. G. Schmidt, Nano Lett. **10**, 3453 (2010).

[61] J. Zabel, R. R. Nair, A. Ott, T. Georgiou, A. K. Geim, K. S. Novoselov, and C. Casiraghi, Nano Lett. **12**, 617 (2012).

[62] W. Pan, J. Xiao, J. Zhu, C. Yu, G. Zhang, Z. Ni, K. Watanabe, T. Taniguchi, Y. Shi, and X. Wang, Sci. Rep. **2**, 893 (2012).

[63] W. Jie, Y. Y. Hui, S. P. Lau, and J. Hao, Appl. Phys. Lett. **102**, 223112 (2013).